Penn Libraries
UNIVERSITY of PENNSYLVANIA

University of Pennsylvania
ScholarlyCommons

Departmental Papers (CBE)

Department of Chemical & Biomolecular Engineering

3-21-2011

Modeling Impedance Response of SOFC Cathodes Prepared by Infiltration

Fred Bidrawn
University of Pennsylvania, fbidrawn@seas.upenn.edu

Rainer Küngas
University of Pennsylvania, kungas@seas.upenn.edu

John M. Vohs
University of Pennsylvania, vohs@seas.upenn.edu

Raymond J. Gorte
University of Pennsylvania, gorte@seas.upenn.edu

Follow this and additional works at: http://repository.upenn.edu/cbe_papers

Part of the Biochemical and Biomolecular Engineering Commons

Recommended Citation

Modeling Impedance Response of SOFC Cathodes Prepared by Infiltration

Abstract

A mathematical model has been developed to understand the performance of electrodes prepared by infiltration of $La_{0.8}Sr_{0.2}FeO_3$ (LSF) and $La_{0.8}Sr_{0.2}MnO_3$ (LSM) into yttria-stabilized zirconia (YSZ). The model calculates the resistances for the case where perovskite-coated, YSZ fins extend from the electrolyte. Two rate-limiting cases are considered: oxygen ion diffusion through the perovskite film or reactive adsorption of O_2 at the perovskite surface. Adsorption is treated as a reaction between gas-phase O_2 and oxygen vacancies, using equilibrium data. With the exception of the sticking probability, all parameters in the model are experimentally determined. Resistances and capacitances are calculated for LSF-YSZ and there is good agreement with experimental values at 973 K, assuming adsorption is rate limiting, with a sticking probability between 10^{-3} and 10^{-4} on vacancy sites. According to the model, perovskite ionic conductivity does not limit performance so long as it is above $\sim 10^{-7}$ S/cm. However, the structure of the YSZ scaffold, the ionic conductivity of the scaffold, and the slope of the perovskite redox isotherm significantly impact electrode impedance. Finally, it is shown that characteristic frequencies of the electrode cannot be used to distinguish when diffusion or adsorption is rate-limiting.

Disciplines
Biochemical and Biomolecular Engineering | Chemical Engineering | Engineering

Modeling Impedance Response of SOFC Cathodes Prepared by Infiltration

F. Bidrawn, R. Küngas,* J. M. Vohs, and R. J. Gorte**,z**

Department of Chemical and Biomolecular Engineering, University of Pennsylvania, Philadelphia, Pennsylvania 19104, USA

A mathematical model has been developed to understand the performance of electrodes prepared by infiltration of $La_{0.8}Sr_{0.2}FeO_3$ (LSF) and $La_{0.8}Sr_{0.2}MnO_3$ (LSM) into yttria-stabilized zirconia (YSZ). The model calculates the resistances for the case where perovskite-coated, YSZ fins extend from the electrolyte. Two rate-limiting cases are considered: oxygen ion diffusion through the perovskite film or reactive adsorption of O_2 at the perovskite surface. Adsorption is treated as a reaction between gas-phase O_2 and oxygen vacancies, using equilibrium data. With the exception of the sticking probability, all parameters in the model are experimentally determined. Resistances and capacitances are calculated for LSF-YSZ and there is good agreement with experimental values at 973 K, assuming adsorption is rate limiting, with a sticking probability between 10^{-3} and 10^{-4} on vacancy sites. According to the model, perovskite ionic conductivity does not limit performance so long as it is above $\sim 10^{-7}$ S/cm. However, the structure of the YSZ scaffold, the ionic conductivity of the scaffold, and the slope of the perovskite redox isotherm significantly impact electrode impedance. Finally, it is shown that characteristic frequencies of the electrode cannot be used to distinguish when diffusion or adsorption is rate-limiting.

In anode-supported solid oxide fuel cells (SOFC), the performance is often limited by the cathode.[1–4] Improving cathode performance could lead to lower operating temperatures, with subsequent improvements in stability. Previously work has demonstrated that improvements can be made in cathode performance through the use of Mixed Ionic and Electronic Conductors (MIEC) in place of purely electronically conductive components,[5–7] by changing the microstructure at the electrolyte interface,[8–10] and through the use of composite electrodes containing an electrolyte material in addition to the electronic conductor.[11,12]

Unfortunately, our understanding of the factors that lead to lower overpotentials in SOFC cathodes is still limited. For example, it is generally accepted that cathode performance should scale with the ionic conductivity of the cathode material.[4,13] However, in studies using composites prepared by infiltrating various perovskites into porous scaffolds of yttria-stabilized zirconia (YSZ), there was no measurable difference in the cathode impedances observed for perovskites with ionic conductivities that differed by as much as 600 times, even though preparation by infiltration methods allowed all of the composites to have similar structures.[14,15] In another example, it is frequently assumed that cathode performance is limited by catalytic properties. However, even though the addition of various promoters has been reported to improve the performance of common cathode materials in some studies,[16,17] our laboratory has determined that the enhancement appears to be due to structural changes in the electrode, rather than to any enhanced catalytic or ion-conduction properties, since inert additives enhanced performance as much as catalytic ones.[14,18] Clearly, there is a need for an improved understanding of the factors that limit SOFC cathode performance.

A considerable number of modeling studies with various degrees of complexity have been carried out to determine the factors that influence electrode properties and to predict electrode performance.[13,20–41] Significant effort has been put into developing a deeper understanding of the mechanisms and rate laws for oxygen exchange on model MIEC surfaces.[3,13,34–39] Taking a step back, models such as those developed by Kenjo et al. and Tanner et al. lump the sophisticated mechanistic steps on the catalyst surface into a single step of dissociative adsorption and are able to provide analytical expressions for potential distribution across simple electrode geometries.[22,41] Extensions to this work are the finite element modeling studies such as those of Nicholas et al.,[25–27] Fleig et al.,[40] and

Lu et al.[21] As a bottom-up alternative to the approach taken by Kenjo et al. and Tanner et al. micro models are based on electrodes consisting of randomly packed spheres.[30–32] The electrical properties of such electrodes are described using the transmission line model. Arguably the most simplistic approach (often applied to the modeling of larger fuel cell systems) is that of fitting and the application of Butler-Volmer kinetics.[20,23,24]

In this study, we build on that background with an overall goal of calculating electrode resistances with at most one fitting parameter. However, it should be noted that the aim of the present work was not to find a best fit to impedance spectra but rather to identify the key trends and variables governing the electrochemical properties of SOFC composite cathodes. Because the best cathodes tend to be composites of an oxide with MIEC and the electrolyte, we have chosen to focus our modeling efforts on composites, using experimental parameters for $La_{0.8}Sr_{0.2}FeO_3$ (LSF) and $La_{0.8}Sr_{0.2}MnO_3$ (LSM) for the MIEC and yttria-stabilized zirconia (YSZ) for the electrolyte. The properties of LSF, LSM, and YSZ are given in Table I. The structure of the composite was chosen to model that of electrodes prepared by infiltration of the MIEC component into a porous scaffold of the electrolyte.[1,25,42–45] These electrodes differ from traditional composites in that both the MIEC and electrolyte phases are well connected within the composite, even at loadings well below those necessary for percolation in random media.[46] However, the performance of electrodes formed by infiltration has many similarities to that of traditional composites,[1] so that the ideas developed here likely apply to traditional composites as well.

Scanning electron microscopy (SEM) images of a porous YSZ scaffold and the LSF-YSZ composites formed by infiltration and calcination to either 1123 or 1373 K are presented in Fig. 1. The images show that the perovskite exists as small particles that uniformly cover the scaffold after heating to 1123 K and that these particles sinter to form a film that appears to coat the YSZ pores after calcination to 1373 K. Results for LSM-YSZ were very similar.[18] Schematic diagrams of the fuel cell and the composite structure are shown in Fig. 2 and are similar to that used by others to model electrode performance.[22,25–27] A diagram of the entire fuel cell is shown in Fig. 2a. Based on the SEM images, we assume that calcination at 1373 K gives rise to dense perovskite films (Fig. 2c), while calcination at lower temperatures causes the perovskites to form smaller particles that cover the YSZ (Fig. 2b).[14,18,45]

Although the performance characteristics of infiltrated LSM-YSZ and LSF-YSZ cathodes depend on whether they are best described by the structure shown in either Figs. 2b or 2c,[14,18,43] cathodes with the film structure shown in Fig. 2c do show

* Electrochemical Society Student Member.
** Electrochemical Society Active Member.
z E-mail: gorte@seas.upenn.edu

Table I. Material Properties of Doped LaFeO₃ and LaMnO₃.
†**Conductivity data for LSM is taken at 1073 K.**

Parameter (Units)	Symbol	Value (Ref)
Ionic conductivity of La$_{0.8}$Sr$_{0.2}$FeO$_{3-\delta}$ (S/cm)	$\sigma_{amb\ LSF}$	8.3×10^{-4} (14)
Ionic conductivity of La$_{0.8}$Ba$_{0.2}$FeO$_{3-\delta}$ (S/cm)	$\sigma_{amb\ LBF}$	3.1×10^{-4} (14)
Ionic conductivity of La$_{0.8}$Ca$_{0.2}$FeO$_{3-\delta}$ (S/cm)	$\sigma_{amb\ LCF}$	3.8×10^{-5} (14)
Ionic conductivity of La$_{0.8}$Sr$_{0.2}$MnO$_{3-\delta}$ (S/cm)	$\sigma_{amb\ LSM}$	4.0×10^{-8} (74)†
Reducibility parameter of La$_{0.6}$Sr$_{0.4}$FeO$_{3-\delta}$	m_{LSF}	-0.034 (63)
Reducibility parameter of La$_{0.6}$Sr$_{0.4}$FeO$_{3-\delta}$	b_{LSF}	0.037 (63)
Reducibility parameter of La$_{0.8}$Sr$_{0.2}$MnO$_{3-\delta}$	m_{LSM}	-0.0077 (61)
Reducibility parameter of La$_{0.8}$Sr$_{0.2}$MnO$_{3-\delta}$	b_{LSM}	-0.039 (61)
Volume of LSF unit cell (Å^3)	V	60.5 (78)

reasonably low impedances at 1073 K,[14,18] despite the fact that, in the strictest sense, there are no three-phase boundary (TPB) sites available. Because modeling the structure in Fig. 2c is significantly simpler, we will focus on this system and discuss the changes that would be expected if the perovskite phase were more particulate in nature. Although Fig. 2b does not show the perovskite particles touching each other, we assume that they are connected electronically.

Considering the picture in Fig. 2c, it is apparent that oxygen transfer from the cathode to the electrolyte will involve gas-phase diffusion of O₂ into the composite, electrochemical oxidation of the perovskite surface, diffusion of the oxygen ions through the perovskite film, and transport of ions down the YSZ fins, all taking place in series. In this paper we assume that gas-phase diffusion is sufficiently fast such that the O₂ concentration is independent of position. This is the usual case for all but the thickest electrodes operating at high current densities.[47]

The step that is most difficult to describe is the oxygen reduction reaction at the perovskite surface. This is most often modeled using the Butler-Volmer equation,[48] which assumes that local field gradients are strong enough to perturb the energies of species along the reaction coordinate. The equation was derived to describe reactions that take place at metal surfaces in solution, where most of the potential drop occurs across a double layer that is approximately 2 nm in thickness,[49] so that field gradients on the order of 1 V/nm are common. These are large enough to significantly alter the reaction coordinate that describes the rate constant. The Butler-Volmer equation indicates that the rate constant should have an exponential dependence on overpotential, so that the cell potential should decrease exponentially with current density near open circuit.

It is not surprising that Butler-Volmer behavior is seen in proton exchange membrane fuel cells (PEM-FC). With PEM-FC, the catalytic metals near the electrolyte interface are effectively immersed in water so as to facilitate transfer of ions into the electrolyte. The situation for SOFC electrodes is far less clear. First, there are many examples in the literature for which the electrode impedance is independent of current density and is the same under cathodic and anodic polarization[14,18,36,50–54] and this current independence has been observed in cells with electrolytes as thin as 15 μm.[55] An example of this is shown in Fig. 3, which is the *V-i* polarization curve for a cell operating under fuel-cell and electrolysis conditions at 973 K, with a 50% CO-CO₂ mixture on the fuel side and an infiltrated LSF-YSZ electrode on air side. Additional details on this cell are given elsewhere[56]; here, we simply note that the constant slope demonstrates the impedances for both electrodes are independent of cur-
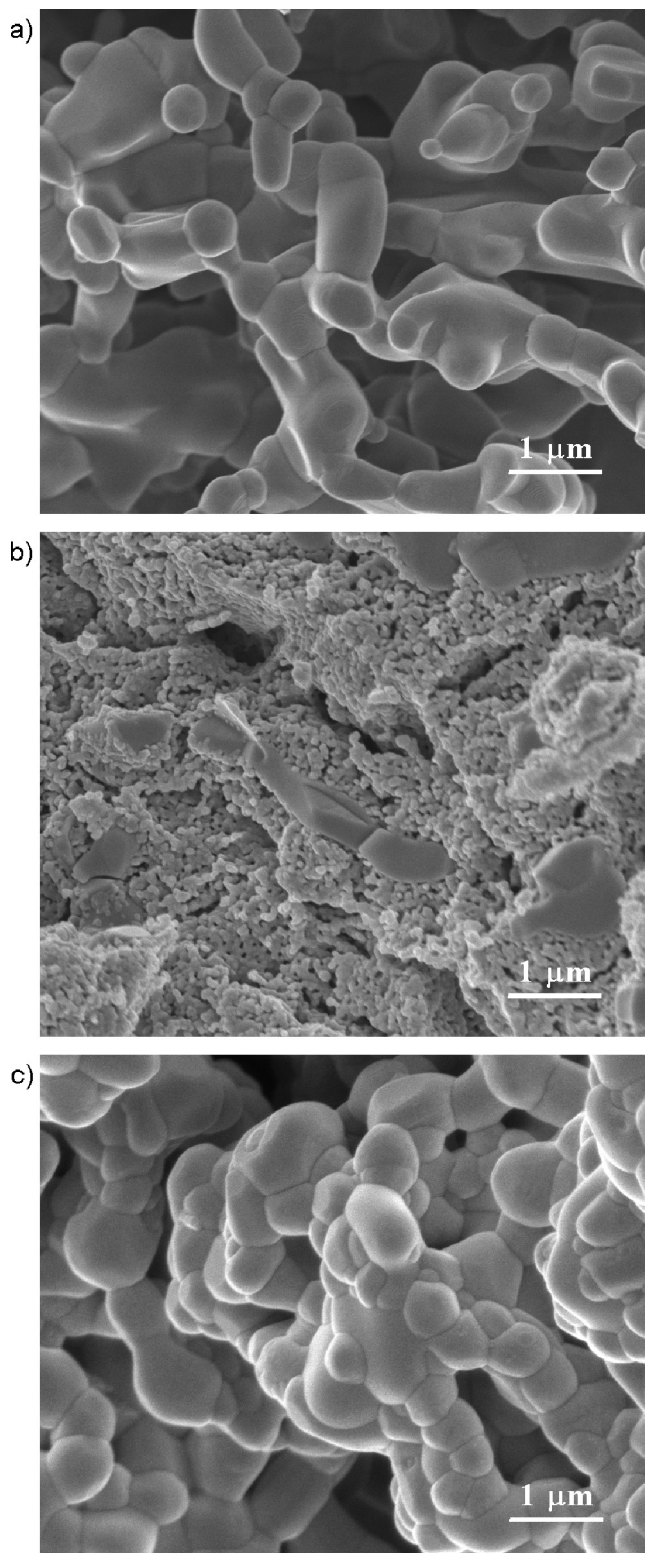
Figure 1. SEM images of (a) the YSZ scaffold used in electrode fabrication, and the 40-wt % LSF-YSZ composites prepared by calcination (b) 1123 K and (c) 1373 K.

rent density and the same under fuel-cell and electrolysis conditions as at open circuit.

While there are also many examples of nonlinear *V-i* curves, it should be noted that the overall shapes of these curve are often significantly different from that predicted by Butler-Volmer.[57,58]
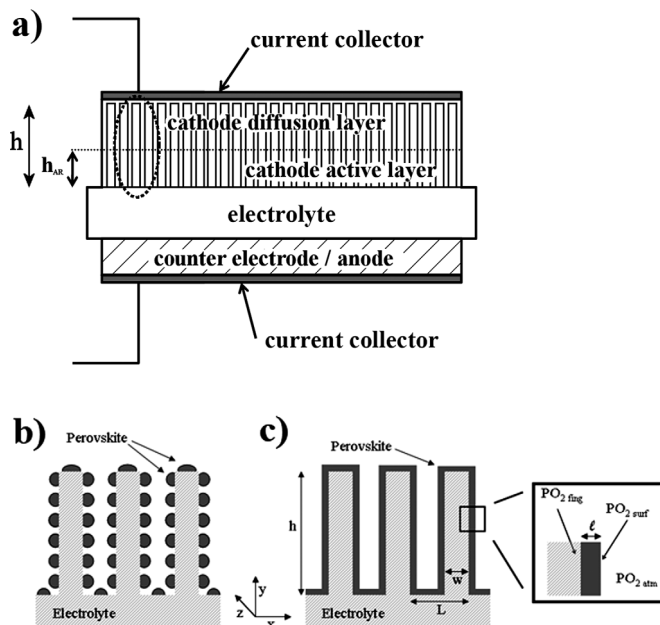
**Figure 2.** Schematic representation of the experimental setup (a), and composite cathodes prepared by infiltration after calcination to (b) 1123 K or (c) 1373 K. Note: h_{AR} is a calculated value determined by electrode properties and refers to the portion of the electrode where overpotential is non-negligible.

Furthermore, there are multiple possible explanations for nonlinear *V-i* curves, such as the hysteretic effects observed with LSM composite cathodes.[44] Second, while field gradients exist in SOFC electrodes, the length scale over which overpotential differences occur is likely much longer than 1 nm; so that field gradients are likely small. Field gradients less than 0.01 V/nm will not significantly affect the barrier height along the reaction coordinate for most reactions. For these reasons, we propose an alternative model of cathode impedance that does not rely on Butler-Volmer kinetics. We recognize that there may be field gradients due to space-charge at the MIEC-air interface that will be important in determining adsorption rate constants but these are not related to overpotential. Finally, although the LSF-YSZ electrodes that we are modeling show identi-
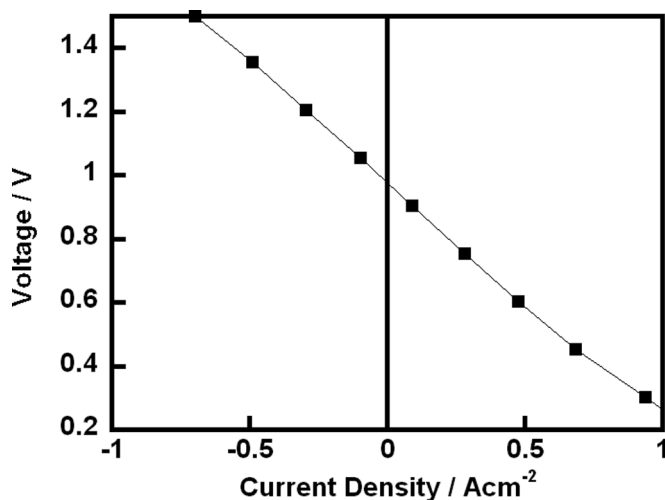
Figure 3. V-i polarization curve for a cell operating under fuel-cell and electrolysis conditions at 973 K. The cell consisted of an infiltrated LSF-YSZ electrode on the air side and was exposed to a 50% CO-CO$_2$ mixture on the fuel side.

cal behavior under cathodic and anodic polarization, there are other cases where differences are observed.

As noted above, we consider two processes as being the most likely to limit the performance of the air electrode: dissociative adsorption of gas-phase O$_2$ onto the perovskite surface and diffusion of oxygen ions through the perovskite film. We treat adsorption as a reaction involving the dissociation of gas-phase O$_2$ onto oxygen vacancies on the surface of the perovskite, with the rate expressed in terms of a surface flux given by the Kinetic Theory of Gases and a reactive sticking coefficient. This sticking coefficient is the probability that an O$_2$ molecule which collides with an oxygen vacancy will then adsorb. Vacancy concentrations in the perovskite are determined from equilibrium data,[3,59–65] so that only the sticking coefficient, a number between 0 and 1, is unknown. Using the model structure presented in Fig. 2c, electrode resistances are calculated based upon experimental parameters determined from characterization of actual cathodes prepared by infiltration. The effects of changing individual parameters are discussed and strategies for improving cathode performance are proposed.

A glossary of symbols and their definitions is presented at the end at the end of this manuscript. We will first present the steady-state models, then solve for the expected electrode resistances for cases where adsorption of O$_2$ is rate-limiting or diffusion of ions through the perovskite film is rate limiting. We will then estimate the capacitances that would be expected for the electrodes in non-steady-state measurements.

Steady-State Model

Structure of the composite electrode.—The cathode geometry presented in Fig. 2c consists of a series of straight YSZ fins of height, *h*, and width, *w*, stemming from the solid YSZ electrolyte and extending to a distance *Z* in the z-direction. Each fin is separated from the next by a distance, *L*. Although these fins are pictured as straight, we incorporate a tortuosity factor, τ. This is in recognition of the fact that the YSZ scaffold of the actual cathode through which the ions will be diffusing could have a complex geometry and a length scale greater than *h*. This tortuosity effectively reduces the ionic conductivity of the YSZ fins by a factor of τ such that

$$\sigma'_{YSZ} = \frac{\sigma_{YSZ}}{\tau} \qquad [1]$$

where σ'_{YSZ} and σ_{YSZ} are the effective and bulk ionic conductivities of YSZ, respectively. It is important to note that we are defining τ for the conduction of ions in the YSZ, not for diffusion in the gas phase.

The parameters defined here can be related to experimental parameters. For example, the tortuosity can be estimated from four probe conductivity measurements on porous slabs.[66] The resulting tortuosity value arises from the network of interconnected YSZ fins (the contribution from dead-end fins is not explicitly accounted for). For straight YSZ fins shown in Figs. 2b and 2c, the conductivity would be that of bulk YSZ multiplied by *(1-p)*, where *p* is the porosity of the YSZ scaffold. The width, *w*, of the fins is the characteristic size of the YSZ scaffold and can be estimated from the SEM in (Fig. 1a). *L*, the characteristic repeat distance in the scaffold, can be related to *w* and *p* from Eq. 2[22]

$$L = \frac{w}{1 - p} \qquad [2]$$

These parameters can also be related to the specific surface area of the YSZ scaffold, S_g, a parameter that can be measured using BET isotherms[44]

$$S_g = \frac{2}{w \rho_{YSZ}} \qquad [3]$$

The perovskite phase is assumed to form a dense film of thickness λ on the YSZ fins. This thickness can be calculated from the weight

Assumption	Introduced
1. YSZ has uniform ionic conductivity, σ_{YSZ}, and negligible electronic conductivity.	Eq. 5
2. Since $w \ll h$, current density within the YSZ fin is a function of y only (fin approximation).	Eq. 5
3. Ion flow through the perovskite film at the top of the fin is negligible (adiabatic tip approximation).	Eq. 7
4. The change in vacancy concentration in the perovskite film is small enough so that σ_{amb} can be considered constant, while the field gradient is still large enough to drive an oxygen flux. In other words, we assume that the ionic conductivity of the perovskite does not change with PO_2.	Eq. 8
5. The electronic conductivity of the perovskite phase is assumed to be very large relative to the ionic conductivity.	Eq. 9
6. Equilibrium exists at the perovskite-YSZ interface. No chemical potential difference exists between current collector and counter electrode, as well as between the counter electrode and the electrolyte at the electrolyte-electrode interface.	Eq. 10
7. The oxygen vacancies on the perovskite surface are identical and independent of each other.	Eq. 12
8. The concentration of oxygen vacancies on the perovskite surface is proportional to δ in $ABO_{3-\delta}$.	Eq. 13
9. Only O_2 molecules impinging on unfilled lattice sites will be able to react with the surface.	Eq. 13
10. Non-stoichiometry δ varies linearly with respect to $\log(PO_2)$.	Eq. 14
11. Particulate electrode (Fig. 2c) can be modeled as a thin-film electrode (Fig. 2b) with an increased surface area for adsorption.	–

percentage of the infiltrated perovskite phase, θ, the density of the perovskite, ρ, and the surface area of the YSZ scaffold.[44]

$$\lambda = \frac{\theta}{(1 - \theta)\rho S_g} \qquad [4]$$

The Potential Within the YSZ Fin

All assumptions used in this model are summarized in Table II. When modeling the electric potential, Φ, within the YSZ fins, we assume that the YSZ has uniform ionic conductivity, σ_{YSZ}, and negligible electronic conductivity. Because the height of the fins is much larger than the width, gradients in the x-direction are assumed negligible, as is ion flow through the perovskite film at the top of the fin. (This is essentially the fin approximation with an adiabatic tip.) Defining $i(y)$ as the current flowing down the fin at any position y and i_S'' as the flux of charge coming into the fin through the perovskite film, the steady-state charge balance becomes Eq. 5

$$2Z\int_{y}^{h} i_s'' dy = i = -\sigma_{YSZ}' wZ \frac{d\Phi}{dy} \qquad [5]$$

The electronic conductivity of the perovskite phase is assumed to be very large, so that the electrical potential of the perovskite phase is fixed. The boundary conditions for Eq. 5 are then given by Eqs. 6 and 7, which simply state that the potential at the electrolyte interface is equal to the cathode overpotential and that there is no current flow from the top of the fin

$$\Phi|_{y=0} = \Phi_0 \qquad [6]$$

$$\frac{\partial \Phi}{\partial y}\Big|_{y=h} = 0 \qquad [7]$$

If we allow h to go to infinity, the condition in Eq. 7 implies that h is greater than the thickness of the electrode active region, h_{AR}, that part of the electrode in which essentially all of the oxygen reduction takes place. Previous work has shown the active region of some state-of-the-art cathodes to be as small as 10 μm (Refs. 8 and 67) although the thickness of the active region will be larger in poorer performing electrodes.

Charge flux through the perovskite film.—To solve Eq. 5, an expression is needed for i_S'', the current flux originating from ions coming through the perovskite film. We will consider two limiting cases: (1) The case where the perovskite surface is in equilibrium with the gas phase and oxygen ion diffusion through the perovskite is limiting; and (2) the case where diffusion through the perovskite film is relatively fast so that oxidation of the perovskite surface is rate limiting. Throughout this manuscript, we assume that the change in vacancy concentration in the perovskite is small enough that the ionic conductivity can be assumed to be constant, whereas gradients in the vacancy concentration are still large enough to drive an oxygen flux.

Diffusion limiting.—The ion diffusion through the perovskite film is given by Eq. 8[14,63]

$$J_{O_2} = \frac{R_g T \sigma_{amb}}{16F^2\lambda} \ln\left(\frac{PO_{2surf}}{PO_{2fing}}\right) \qquad [8]$$

Here, PO_{2surf} and PO_{2fing} correspond to the oxygen fugacities at the film surface in contact with the atmosphere and with the YSZ fin, respectively. σ_{amb} is the ambipolar conductivity of the perovskite as defined by Eq. 9 (Refs. 14 and 63) and is assumed to be constant

$$\sigma_{amb} = \left(\frac{\sigma_i \sigma_{el}}{\sigma_i + \sigma_{el}}\right) \qquad [9]$$

For materials with much higher electronic than ionic conductivities, as are the cases for LSF and LSM, the ambipolar conductivity is essentially equal to the ionic conductivity. For the case where diffusion of ions through the perovskite film is rate-limiting, PO_{2surf} is simply 0.21 atm. We assume equilibrium exists at the perovskite-YSZ interface, so that PO_{2fing} can be related to the potential within the YSZ fin using the Nernst equation

$$\Phi = \frac{R_g T}{4F} \ln\left(\frac{PO_{2atm}}{PO_{2fing}}\right) \qquad [10]$$

In Eq. 10, we implicitly also assume that there is no material difference between current collector and counter electrode, as well as no difference between the counter electrode potential and that of the electrolyte at the point of contact with the counter electrode. By combining Eqs. 8 and 10, the flux of oxygen ions through the perovskite film at any position can be directly related to the electric potential within the YSZ fin.

Finally, the oxygen flux can be related to i_S'' through Eq. 11 (Ref. 63)

$$i_S'' = 4F J_{O_2} \qquad [11]$$

Surface reaction limiting.—Although the dissociative adsorption rate of O_2 onto the perovskite surface could have been written in terms of surface-exchange rates, this formalism would not have allowed the rates to be expressed in terms of the oxidation state of the surface. Therefore, for the surface reaction-limited case, we assume that oxygen incorporation into the perovskite can be treated as a reaction between gas-phase O_2 and the oxygen vacancies in the perovskite lattice. If the vacancies are identical and independent of each other, the rate per area of surface will be proportional to the

collision frequency between gas molecules and the surface and given by Eq. 12

$$r_{ads} = \frac{PO_{2atm}}{(2\pi MR_gT)^{1/2}} \cdot S \qquad [12]$$

Here, S is the sticking coefficient, the probability that a molecule striking the surface will adsorb. Because a molecule must find a vacancy site in order to react, the sticking coefficient will depend on the vacancy concentration of the perovskite and a vacancy sticking probability, S_0.

For a perovskite of composition $ABO_{3-\delta}$, it is reasonable to suggest, as a first approximation, that

$$S = S_0 \left(1 - \frac{3-\delta}{3-\delta_0} \right) \qquad [13]$$

where S_0 is a constant at any given temperature and the term in parenthesis is the fraction of oxygen lattice sites that are vacant in the bulk. We are assuming here that only O_2 molecules impinging on unfilled lattice sites will be able to react with the surface. Although S may depend on the square of the vacancy concentration for dissociative adsorption (i.e. adsorption of an O_2 molecule will require two available sites, one for each oxygen atom.), we treat the dependence of S on the vacancy concentration as linear for simplicity in order to obtain an analytical solution. Furthermore, adsorption of non-dissociative molecular O_2 is known to be the rate limiting step for CO oxidation on Pt,[68] so that Eq. 13 may indeed be a better description of the actual kinetics. Although we recognize that oxygen adsorption rates in SOFC are more typically described using an exchange coefficient, k^*, the advantage of using a sticking coefficient is that it allows us to define a rate constant, S_0, that is not dependent on PO_2. It is noteworthy that k^* has been shown to vary with PO_2 in ways that correlate with bulk oxygen vacancy concentrations in perovskite cathodes, an observation that supports the validity of the assumption made in Eq. 13.[69]

At equilibrium, δ will be a function of stoichiometry, temperature, and PO_2. For most materials of interest for SOFC cathode applications, δ varies almost linearly with respect to $\log(PO_2)$ over the range of interest for SOFC cathodes, $1 > PO_2 > 10^{-5}$ atm, as demonstrated by the thermodynamic data for LSM, LSF, and LSCo presented in Fig. 4.[60,62,63] Therefore, we express the concentration of oxygen vacancies at the perovskite surface using Eq. 14
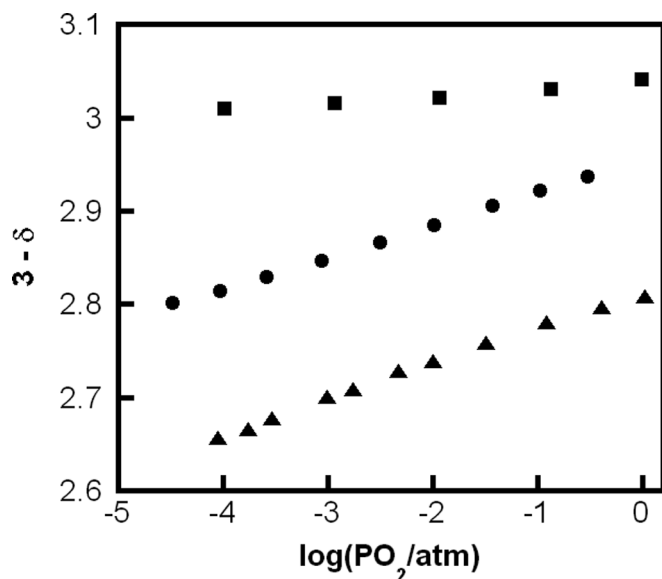

Figure 4. The PO_2 dependence of the oxygen non-stoichiometry of (■) $La_{0.8}Sr_{0.2}MnO_{3-\delta}$,[61] (●) $La_{0.6}Sr_{0.4}FeO_{3-\delta}$,[63] and (▲) $La_{0.3}Sr_{0.7}CoO_{3-\delta}$.[60]

$$\delta = m\log(PO_2) + b \qquad [14]$$

Here, m and b are the slope and intercept of a plot of δ versus $\log(PO_2)$. From Fig. 4, it can be seen that m and b vary widely with perovskite composition. Upon combining Eqs. 12, 13, and 14, the adsorption rate can be expressed as follows

$$r_{ads} = \frac{PO_{2atm}S_0}{(2\pi MR_gT)^{1/2}} \cdot \frac{m\log(PO_{2surf}) + b}{3} \qquad [15]$$

When rates are limited by surface adsorption (i.e. diffusion of ions through the perovskite film is relatively fast), the surface vacancy concentration will be equal to that of the bulk and PO_{2surf} will be equal to PO_{2fing}.

In the absence of ion flow (open-circuit conditions for the electrode), there will be an equilibrium vacancy concentration corresponding to the PO_{2atm} of the gas phase within the electrode. Because O_2 desorption must balance O_2 adsorption in order to establish this equilibrium, we define this equilibrium desorption as the adsorption rate at PO_{2atm}. If we assume that lattice oxygen sites are equivalent and that changes in δ are small, it is reasonable to assume that the desorption rate, r_{des}, is constant and given by Eq. 16

$$r_{des} = \frac{PO_{2atm}S_0}{(2\pi MR_gT)^{1/2}} \cdot \frac{m\log(PO_{2atm}) + b}{3} \qquad [16]$$

As with the diffusion-limited case, the adsorption rate can then be related to the potential at any position along the YSZ fin and the net rate of adsorption can be related to i_S'' through Eq. 17

$$i_S'' = 4F(r_{ads} - r_{des}) \qquad [17]$$

Analytical, Steady-State Solutions

Because the net rate of oxygen adsorption at the gas-phase surface of the perovskite film must equal the flux of ions through the film, Eqs. 8 and 15 can be combined to solve for the oxygen fugacity of the perovskite at the gas-phase surface, Eq. 18

$$\log P_{O_{2surf}} = \frac{\frac{A}{B}\ln P_{O_{2fing}} - m\log(P_{O_{2atm}})}{\frac{A}{B}\log e - m} \qquad [18]$$

In this equation, there is no assumption as to whether the rate is limited by adsorption or diffusion; A and B are the prefactors for the diffusive flux and adsorption rate, respectively

$$A = \frac{R_gT\sigma_{amb}}{16F^2\lambda} \qquad [19]$$

and

$$B = \frac{S_0P_{O_{2atm}}}{3\sqrt{2\pi MRT}} \qquad [20]$$

The relative magnitude of A and B determines which process is rate limiting. If A is much larger than B, PO_{2surf} will become equal to PO_{2fing} and surface adsorption is rate limiting. Conversely, if B is much larger than A, diffusion is the rate limiting process and PO_{2surf} will become equal to PO_{2atm}. We consider the analytical solutions for the expected electrode resistances for each of these limiting cases separately.

Diffusion limited.— By combining Eqs. 8, 10, and 11, the oxygen flux can be related to chemical potential at any given point in the YSZ fin, allowing one to solve for i_S'' at any position along the fin,

providing an expression for the amount of current entering the YSZ fin at a given point

$$i_S'' = \frac{\sigma_{amb}}{\lambda}\Phi|_y \qquad [21]$$

Solving Eq. 5 using the boundary conditions specified in Eqs. 6, 7 (with $h = \infty$), and 21 provides expressions for the potential and the total current within the YSZ fin. From these, the DC electrode resistance, R, can be calculated from the ratio between the overpotential and the current. These solutions are shown in Eqs. 22 through 24

$$\Phi(y) = \Phi_0 \exp\left(-y\sqrt{\frac{\sigma_{amb}}{\frac{w}{2}\lambda\sigma_{YSZ}'}}\right) \qquad [22]$$

$$i(y) = (1-p)\sqrt{\frac{\sigma_{amb}\sigma_{YSZ}'}{\frac{w}{2}\lambda}}\Phi(y) \qquad [23]$$

$$R = \frac{1}{(1-p)}\sqrt{\frac{\frac{w}{2}\lambda}{\sigma_{amb}\sigma_{YSZ}'}} \qquad [24]$$

Although these results will be discussed more in depth later, it is worth noting that the dependence of the resistance upon $\sigma_{amb}^{-1/2}$ is analogous to the result found by Adler and coworkers[13] when modeling the impedance of a porous layer of a mixed conducting material on a flat electrode.

Surface adsorption limited.—The potential gradient within the YSZ fin for the case where surface adsorption is rate limiting can be obtained in the same manner as the diffusion-limited case, and the analytical solution takes a similar form. Combining Eqs. 10, 15, 16, and 17 with large A/B (such that PO_{2surf} equals PO_{2fing}) results in the following expression for i_S''

$$i_S'' = E\frac{mS_0}{3}\Phi|_y \qquad [25]$$

where E is a simplifying collection of constants:

$$E = \frac{-16F^2 P_{O_{2atm}}\log(e)}{(2\pi M)^{1/2}(R_g T)^{3/2}} \qquad [26]$$

Substituting this expression into Eq. 5 and again using the boundary conditions specified in Eqs. 6 and 7 (for $h = \infty$), we obtain expressions for the potential in the YSZ fin, the total current from each fin, and the overall electrode resistances, Eqs. 27 through 29

$$\Phi(y) = \Phi_0 \exp\left(-y\sqrt{\frac{E \cdot mS_0}{3\frac{w}{2}\sigma_{YSZ}'}}\cdot\right) \qquad [27]$$

$$i(y) = (1-p)\sqrt{\frac{E \cdot mS_0\sigma_{YSZ}'}{3\frac{w}{2}}}\Phi(y) \qquad [28]$$

$$R = \frac{1}{(1-p)}\sqrt{\frac{3\frac{w}{2}}{E \cdot mS_0\sigma_{YSZ}'}} \qquad [29]$$

An important conclusion from this result is that the electrode resistance depends primarily on the slope, m, of the equilibrium, redox isotherm for the perovskite. This suggests that more reducible materials should show lower resistances.

For both the diffusion-limited case, Eq. 24, and the adsorption-limited case, Eq. 29 the electrode impedance depends on structural properties (porosity and fin size) and the dependencies shown are similar to those proposed previously by Tanner, et al.[22] Both results also show an inverse square-root dependence of the electrode resistance on the ionic conductivity of the electrolyte scaffold. This suggests that

the use of composites with an electrolyte of higher ionic conductivity (i.e. Gd-doped ceria) should decrease the impedance regardless of whether adsorption or diffusion is limiting. Finally, it is interesting to consider that the resistances obtained for both cases should not depend on the direction of the currents, so that impedances for electrodes operating cathodically or anodically should be the same, as we have already observed is often the case experimentally, as in Fig. 3.

Effect of Perovskite Structure

It is interesting to consider the case where the perovskite particles are more particulate in nature, similar to that shown diagrammatically in Fig. 2b, rather than film-like. Equations 5 through 7 which describe the potential in the YSZ fin would remain unchanged from the film case described above. Only the expression for i_S'' would be affected. Coming up with an expression for i_S'' in this situation is now more difficult. Considering just an individual perovskite particle on the YSZ surface, the picture is essentially that which is commonly used in modeling TPB sites.[21] There will now be sites where the perovskite particle, the YSZ, and the gas phase all come into contact. In principle, O_2 molecules could adsorb on the perovskite particles at sites far from the TPB sites and then diffuse to the YSZ interface, either through the bulk or along the perovskite surface.

For the case where adsorption of O_2 is rate limiting, the entire perovskite particle will be at the same chemical potential, determined by the potential of the YSZ at that position along the fin. The solutions given in Eqs. 27–29 would apply to this case, except that there would now be an increased surface area for adsorption. The surface area in the rate expression of Eq. 12 is accounted for only in the perimeter of the YSZ fin. Depending on whether oxygen ions can be transferred between adjacent perovksite particles (Contact is required for electrical conduction.), the available surface area could be that of the particles in contact with the YSZ or could include particles that are only in contact with the YSZ through their interaction with other particles.

For the diffusion-limited case, the question is the relative importance of TPB sites compared to that of the bulk sites at the point of contact between the perovskite particles and the YSZ. For the "bulk" sites, Eqs. 22 through 24 still approximately apply, although the relevant length scale for diffusion, λ, would now be the particle size. For both the diffusion-limited and surface-adsorption-limited cases, the electrode impedances are expected to be smaller for the particulate case.

Non-Steady State Solutions

The framework developed in the previous sections can also be used to model the time response of the system to sudden changes in the cathode overpotential. Rather than using the steady-state approximation for the permeation flux through a thin perovskite film as specified in Eq. 8, the flux entering the YSZ fin, which is related to i_S'' through Eq. 11, can be expressed in terms of the oxygen-ion concentration gradient by the tracer self-diffusion coefficient, D, such that[3]

$$J_{O_2} = D\frac{\partial C(t)}{\partial x} \qquad [30]$$

The ionic conductivity can then be expressed in terms of the diffusion coefficient D and the stoichiometry parameter, δ, as shown in Eq. 31[63]

$$\sigma_i = D\frac{16F^2}{RTV}\delta \qquad [31]$$

where V is the volume of the perovskite unit cell. Substituting Eq. 14 into 31, we obtain

$$\sigma_i = D\frac{16F^2}{RTV}(m\log pO_2 + b) \qquad [32]$$

It is important to note that the relationship between σ_i and D includes a dependence on m, the reducibility parameter. The time-dependent, oxygen-ion concentration profile within the film was then modeled using a one-dimensional form of Fick's second law of diffusion[3]

$$\frac{\partial C}{\partial t} = D \frac{\partial^2 C}{\partial x^2} \qquad [33]$$

J_{O_2} can again be expressed in terms of i_S'' through Eq. 11. At the interface between the perovskite and the YSZ fin, a pair of matching conditions was used such that the chemical potential in the film and the fin were equal and that the fluxes of ions leaving the film and entering the fin were equal. At the perovskite surface in contact with the gas phase, net O_2 adsorption was again modeled according to Eqs. 15 and 16.

Electrochemical impedance spectroscopy (EIS) is a powerful technique that can provide information for identifying these different processes. These measurements can be performed either through sine wave testing or through current- or potential-step techniques, both of which provide identical information about the system being tested. Sine wave testing typically consists of applying a sinusoidal current perturbation and measuring the phase-shifted potential response of the system. The complex frequency domain impedance, $Z(\nu) = \Phi(\nu)/i(\nu)$, is measured across a range of frequencies and presented on a Nyquist plot. Similarly, a potential step can be applied to the system while the current response is measured. Frequency domain data, identical to that which would be measured using sine wave testing, can then be obtained by performing a Fourier Transform of the time-dependent current and voltage profiles, $i(t)$ and $\Phi(t)$, followed by complex division.[70-73]

For the simulations in this work, we modeled the current responses to step changes in the cathode overpotential. For $t < 0$, the system was assumed to be at "open-circuit" voltage, with no overpotential applied to the YSZ fin. Because the system was considered at equilibrium, the vacancy concentration everywhere within the perovskite was set equal to C_0, the concentration of oxygen ions at PO_{2atm}, corresponding to an overpotential of 0 V. Beginning at $t = 0$, the overpotential at the base of the YSZ fin was set equal to Φ_0. Following this step change in potential, the current responses were calculated until new steady states were reached. Representative examples of the potential step, with a $\Phi_0 = 0.01$ V, and the resulting current response are provided in Fig. 5, as well as the corresponding Nyquist plot, shown in Fig. 6. By integrating the current response of the system over time, the capacitances were obtained. Because this model incorporated both oxygen adsorption at the perovskite surface and diffusion through the perovskite film, it allowed the calculation of resistances and capacitances for co-limited cases as well as the purely diffusion or adsorption limited cases addressed previously. Since these results were obtained numerically, they will be presented in the next section for various ranges of parameters.

Model Implications and Example Calculations

In this section, we examine the implications of this model for typical experimental conditions. Unless otherwise noted, all calculations use the thermodynamic and conductivity parameters presented in Table I and the structural parameters presented in Table III.

Electrodes based on infiltrated LaFeO₃.—Figure 1b shows an SEM micrograph of an LSF-YSZ electrode prepared by infiltration of 40-wt % LSF into a YSZ scaffold that was 66% porous, after calcination to 1373 K.[14] This electrode was prepared as part of a study in which LaFeO₃-based electrodes were synthesized with Ca, Sr, and Ba as dopants in order to examine the effect of changes the ionic conductivities.[14] A related study of infiltrated LaNi₀.₆Fe₀.₄O₃ and La₀.₉₁Sr₀.₀₉Ni₀.₆Fe₀.₄O₃ was carried out with the same YSZ scaffold and treatment conditions.[15] Of particular importance here is the fact that all of the parameters from our calculations, with the
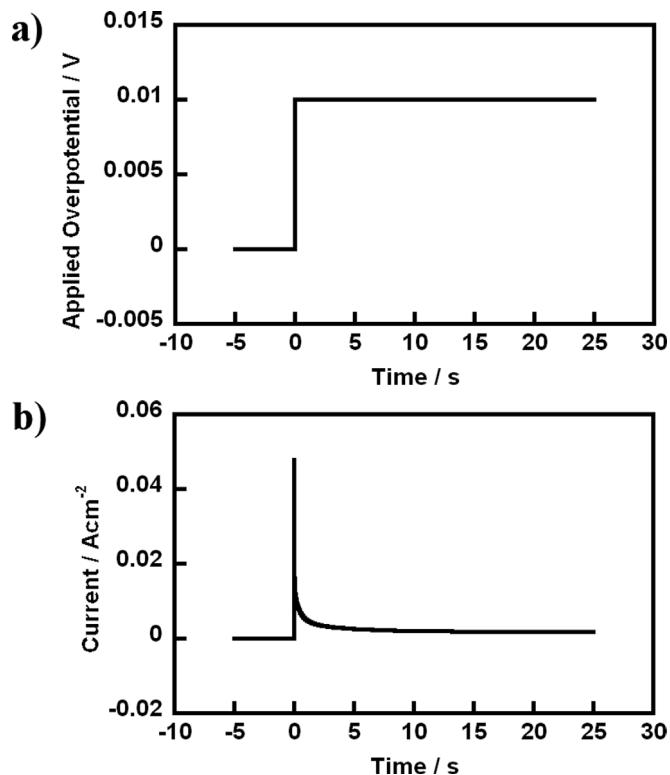
Figure 5. Representative time-profiles for the a) applied overpotential step function and the b) resulting current response for the non-steady state, co-limited model based on the parameters listed in Table III at 973 K. This example case used $S_0 = 10^{-4}$ and $D = 10^{-13}$ cm²/s.

exception of S_0, have been measured in the characterization of these electrodes.

The impedances of electrodes made with all of the above perovskites, at 973 K in air, depended on current density; but, at open circuit, the impedances of the electrodes calcined at 1373 K were ~3 $\Omega \cdot$cm². The impedances did not show the logarithmic dependence that would be expected for Butler-Volmer behavior[45] and the differences in the open-circuit impedances after calcination to 1373 K appear to be within the variability of different measurements.[14,18]

If the electrodes were limited by oxygen-ion diffusion through a dense perovskite film, the resistances can be calculated using Eq. 24. Using the parameters from Table I, the anticipated electrode impedances would vary from 0.06 $\Omega \cdot$cm² with LSF-YSZ electrodes to 0.3 Ω cm² for the LCF-YSZ electrodes as shown in Table IV. Since one would expect this calculation to overestimate the resistance, given that the experimental perovskite films are almost certainly not perfectly dense, the fact that the measured impedances are significantly larger than the values predicted by the diffusion-limited calculation implies that diffusion limitations are likely not important. Another way of looking at the issue is to calculate what the ionic conductivity would have to be in order for the electrodes to exhibit an impedance of 3 Ω cm². Based on Eq. 24, the parameters in Table III, σ_{amb} would have to be less than 10^{-7} S/cm. Although doped LaFeO₃ species have ionic conductivities much greater than this value, studies have shown LSM to have a significantly lower ionic conductivity.[74] This lower ionic conductivity suggests that LSM-YSZ electrodes may be limited by diffusion. This provides a possible explanation as to why LSM shows higher impedances compared to doped LaFeO₃.[18,75] Figure 7 shows the resistance as a function of perovskite and YSZ ionic conductivity for the diffusion limited case as calculated by Eq. 24.

If one assumes that the adsorption rate is limiting and that the vacancy concentrations at a given PO_2 are similar across this set of samples, Eq. 29 can be used to estimate a sticking coefficient for the
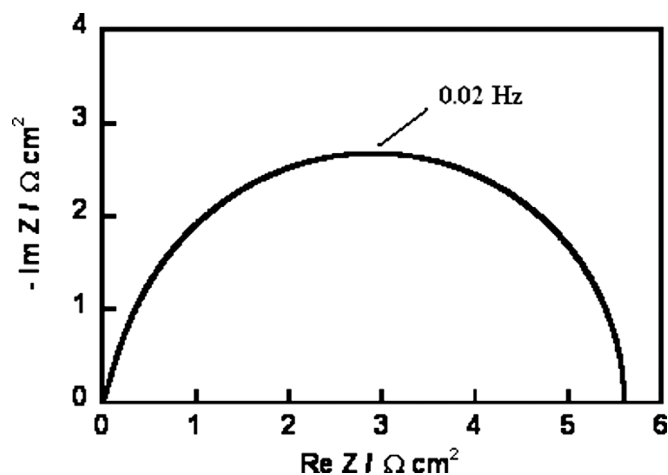
Figure 6. The corresponding Nyquist plot for the data presented in Figure 5.

vacancy sites, S_0. As shown in Fig. 8, using an electrode resistance of 3 Ω cm^2 and the parameters in Tables I and III, S_0 is calculated to be $\sim 10^{-4}$, a reasonable value for a reactive sticking probability. This, along with the fact that the resistances did not change with ionic conductivity in this series, suggests that the performance of the infiltrated LaFeO$_3$-based electrodes was limited by adsorption.

As noted previously, when modeling dissociative adsorption, S is typically assumed to depend on the square of the vacancy concentration, effectively replacing Eq. 13 with Eq. 34

$$S = S_0 \left(1 - \frac{3 - \delta}{3 - \delta_0}\right)^2 \qquad [34]$$

Because the δ is of the order ~ 0.1 for overpotentials between 0.1 and 0.2 V in LSF, the presence of this additional term would require that the value of S_0 increase by a factor of 30 to obtain resistances of ~ 3 Ω cm^2. It is also worth noting that the use of Eq. 34 will also introduce a non-linearity into the resulting V-i curve. For example, when using a S_0 of 30×10^{-4} and the parameters specified in Tables I and III, the calculated resistances are ~ 3 Ω cm^2 at an overpotential 0.01 V and ~ 2 Ω cm^2 at an overpotential of 0.25 V. This suggests that dissociative adsorption may be a cause of the nonlinear V–I curves sometimes seen experimentally.

When calcined at only 1123 K, all of the LaFeO$_3$-based electrodes showed perovskite particles that were particulate in nature, rather than film-like, similar to that shown in Fig. 2b. All of these electrodes exhibited a current-independent impedance of 0.2 Ω cm^2 at 973 K.[6] As discussed earlier, the particulate nature of the infiltrated perovskites would be expected to affect both the diffusion-limited and the adsorption-limited case, so that this observation cannot be used to infer which process is limiting. However, if diffusion is not limiting for the electrodes calcined at 1373 K, diffusion limitations will certainly not be a factor for 1123-K electrodes, given that the length scale for diffusion will be much smaller.

Table III. Structural Parameters for Typical Composite Cathode.

Parameter (Units)	Symbol	Value
Fin width (μm)	w	1
Electrode porosity	p	0.66
Perovskite film thickness (μm)	λ	0.26
Electrode thickness (μm)	h	50
Tortuosity factor	τ	7
Ionic conductivity of YSZ at 973 K (S/cm)	σ_{YSZ}	2.0×10^{-2}
Effective Ionic conductivity of YSZ at 973 K (S/cm)	σ'_{YSZ}	2.9×10^{-3}

Table IV. Example calculations based on the diffusion limited case at 973 K. †Conductivity data for LSM is taken at 1073 K.

Composite	σ_{amb} (S/cm) (Ref)	σ'_{YSZ} (S/cm)	Calculated Resistance at 973 K(Ω cm^2)	Measured Impedance at 973 K (Ω cm^2) (Ref)
LSF-YSZ	8.3×10^{-4} (14)	0.0029	0.067	2.8 (18)
LBF-YSZ	3.1×10^{-4} (14)	0.0029	0.11	2.9 (14)
LCF-YSZ	3.8×10^{-5} (14)	0.0029	0.31	3.0 (14)
LSM-YSZ	4.0×10^{-8} (74)†	0.0029	9.7	8.8 (75)

Comparison of sticking coefficient to alternate rate expressions.— In SOFC, O$_2$ adsorption rates are most commonly presented in terms of the exchange coefficient, k^*, or exchange current density, i_0, rather than a sticking coefficient. Values of k^* are typically determined from isotope exchange experiments[63] and can be related to oxygen adsorption through the relation

$$r_{ads} = k^*(C_{A0} - C) \qquad [35]$$

where k^* has units of cm/s, and C_{A0} is the oxygen concentration of the surface in equilibrium with the gas. Literature values of k^* range from $\sim 5 \times 10^{-4}$ cm/s at 973 K for La$_{0.6}$Sr$_{0.4}$FeO$_{3-\delta}$ (Ref. 59) to $\sim 10^{-9}$ cm/s (Ref. 76) at 973K for La$_{0.8}$Sr$_{0.2}$MnO$_{3-\delta}$. By substituting Eqs. 13 and 35 into Eqn. 12, and accounting for units, S_0 can be shown to be approximately 50 times k^*. It is interesting to notice that k^* values reported in the literature correspond to S_0 values in the range of $10^{-2} - 10^{-7}$, which are in general agreement with the value of $S_0 = 10^{-4}$ coming out of our calculations.

Exchange current densities are sometimes used as fitting parameters in the Butler-Volmer expression and correspond to the forward and reverse reaction rate at equilibrium. By substituting Eqs. 13 and 14 into Eq. 12 and assuming $PO_2 = PO_{2atm}$ at equilibrium, an S_0 value of the 10^{-4} can be shown to correspond to an i_0 of 1.3 mA/cm^2. This value is somewhat lower than the $i_0 = 300$ mA/cm^2 reported in the literature for LSF at 973 K.[77]

Thickness of the electrochemically active region.— The analytical solutions for the adsorption- and diffusion-limited cases were derived assuming the electrodes were infinitely thick. It is therefore of interest to relax the assumption of an infinitely thick electrode
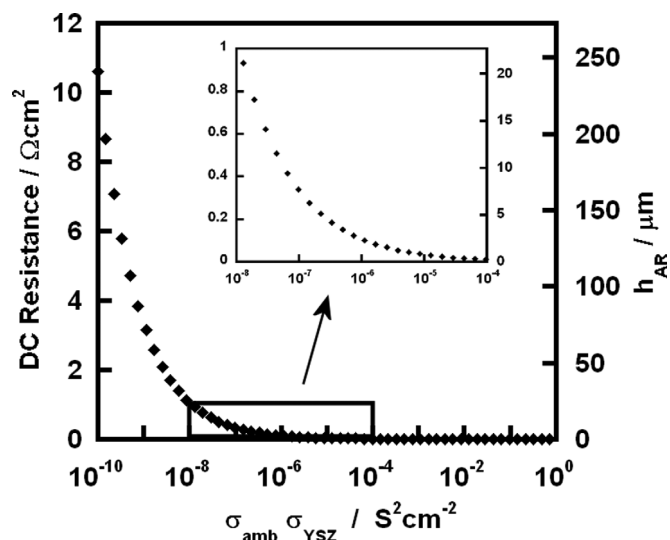

Figure 7. DC resistance as a function of perovskite and YSZ ionic conductivity for the diffusion limited case as calculated by Eq. 24 using the parameters outlined in Table III and $h = \infty$. The secondary axis illustrates the thickness of the active region for a given resistance using $\sigma'_{YSZ} = 0.0029$ S/cm.
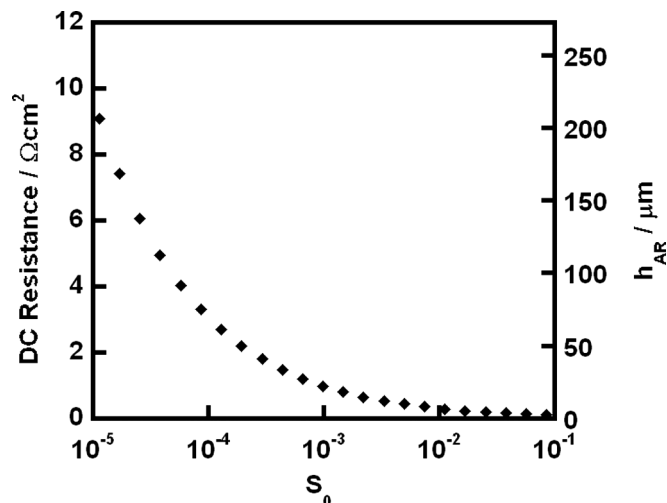
Figure 8. DC resistance as a function of perovskite and YSZ ionic conductivity for the diffusion limited case as calculated by Eq. 29 using the parameters outlined in Table III and $h = \infty$. The secondary axis illustrates the thickness of the active region for a given resistance using $\sigma'_{YSZ} = 0.0029$ S/cm.

Figure 9. Potential profile within the YSZ fin for an applied overpotential of 0.2 V and electrode thicknesses, h, of (■) 100, (●) 50, and (▲) 20 μm. Profiles are based upon the adsorption limited case with a S_0 value of 10^{-4} and the parameters listed in Table III. Calculated resistances are provided for each electrode thickness.

and determine the thickness of the active region, where the majority of the electrochemical reaction takes place. Equations 22 and 27 indicate that electrical potential within the YSZ fins decreases exponentially; when the electrical potential in the YSZ is zero, there is no potential driving force for oxygen transport through the perovskite. Defining h_{AR} as the distance into the electrode at which the potential is 10% of the total electrode overpotential, it can be shown through manipulation of Eqs. 22 and 24 or 27 and 29 that

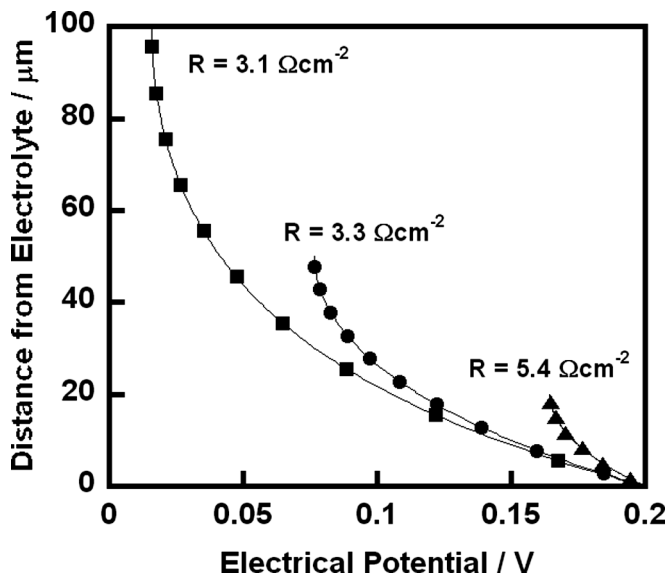$$h_{AR} = -\ln(0.1)\sigma'_{YSZ}R(1-p) \qquad [36]$$

For a measured impedance of 0.3 Ω cm^2 using porosity values provided in Table III, this equation predicts that the active region will be $\sim$7 μm thick. This is in good agreement with literature reports that have determined the active region to be on the order of 10 μm thick.[8,67]

When the electrode thickness is less than h_{AR}, the electrode impedance will be greater than that calculated from Eqs. 24 or 29, and Eq. 5 must be solved with the appropriate value of h for the boundary condition in Eq. 7. To demonstrate the effect that thinner electrodes can have, we present results from a calculation in which adsorption is assumed to be rate limiting, with S_0 equal to 10^{-4}. Using the physical parameters listed in Table III, the electrode impedance for an infinitely thick electrode is determined to 3.1 Ω cm^2 and h_{AR} is found to be $\sim$65 μm from Eq. 36. Figure 9 shows numerically calculated results for the potential within the YSZ fins for electrodes having thicknesses of 20, 50, and 100 μm, assuming an overpotential of 0.2 V. For an electrode that is 100 μm thick, the potential profile is very similar to that which would be observed for an infinitely thick electrode and the electrical potential at the tip of the YSZ fin is approximately 0.02 V. The calculated impedance is identical to that obtained from Eq. 29, 3.1 $\Omega \cdot$cm^2. For the 20- and 50-μm electrodes, the potentials within the electrode deviate from that of Eq. 27 but the calculated resistances, 3.33 and 5.42 $\Omega \cdot$cm^2, were significantly different only for the 20-μm electrode.

Non-Steady State Solutions

In the following sections, we used the time-dependent equations to examine the effects of D and S_0 on the electrode resistances and capacitances. The work in this section assumes an electrode thickness of $h = 50$ μm.

Diffusion and adsorption co-limited resistances.—To determine what the effect would be of having diffusion and adsorption be co-

limiting, we calculated electrode resistances from the solution to the non-steady-state equations after long times. The results for typical experimental parameters from Table III are shown in Fig. 10 as a function of the diffusion coefficients and sticking coefficients. As expected, for a given value of D, the diffusion-limited case gives the lowest possible impedance and this minimum value decreases as D increases. Figure 10 also illustrates that for a given sticking coefficient, once the diffusion coefficient is sufficiently large and diffusion is no longer limiting, the impedance becomes independent of D.

Calculated capacitances.—Characterization of electrode performance by impedance spectroscopy measures the time response of the electrode to changes in the input. The capacitance of the electrode is measured in addition to the electrode impedance. To determine expected electrode capacitances for our model, we numerically calculated the current response to step changes in the overpotential from $\Phi = 0$ to 0.01 V. This step change caused spikes in current density, which then relaxed to the steady-state currents expected for the steady-state electrode resistances. The area under the plot of current-versus-time was used to calculate the capacitance, similar to what would be done experimentally in current-interrupt measurements. It should be noted that we have ignored double-layer capacitances that can be found at rate-limiting air-MIEC interfaces.

Figure 11 shows the calculated capacitances as a function of both D and S_0, again using physical parameters from Table III. As with the calculated resistances in Fig. 10, the purely diffusion-limited case provides the minimum capacitance value for a given D. For the cases where the adsorption rate becomes limiting, the calculated capacitance decreases as the sticking coefficient decreases. For a given S_0, the capacitance values are fairly constant and the adsorption and diffusion co-limited regions are not as easily identifiable as they were from Fig. 10.
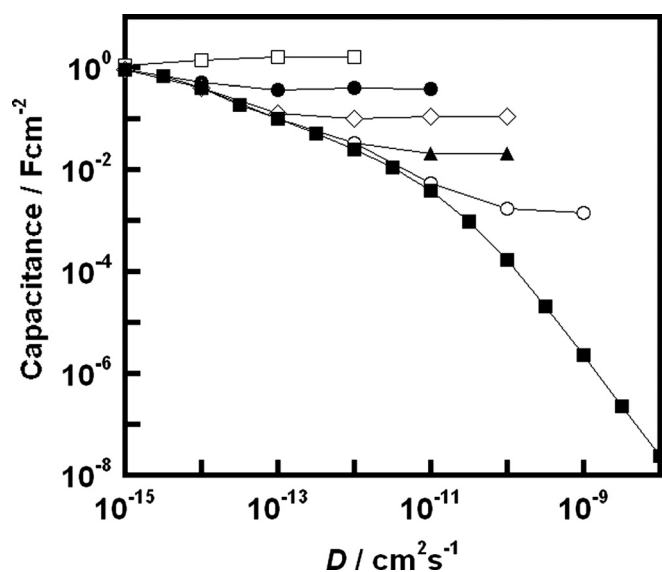
Analysis of non-steady state solutions.—From the results in Figs. 10 and 11, it is possible to calculate the characteristic frequency for the electrode. Often, electrode impedances are modeled using equivalent RC circuits such that the characteristic frequency, f, can be related to the low-frequency intercept, R, and the electrode capacitance, C_p, by
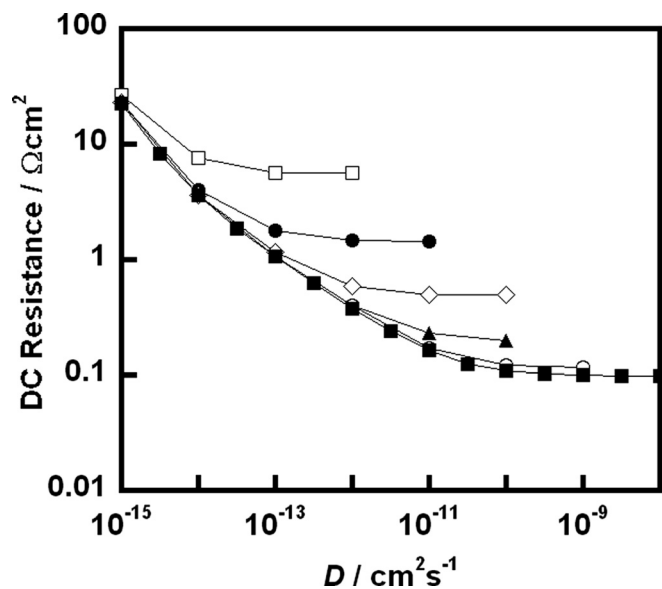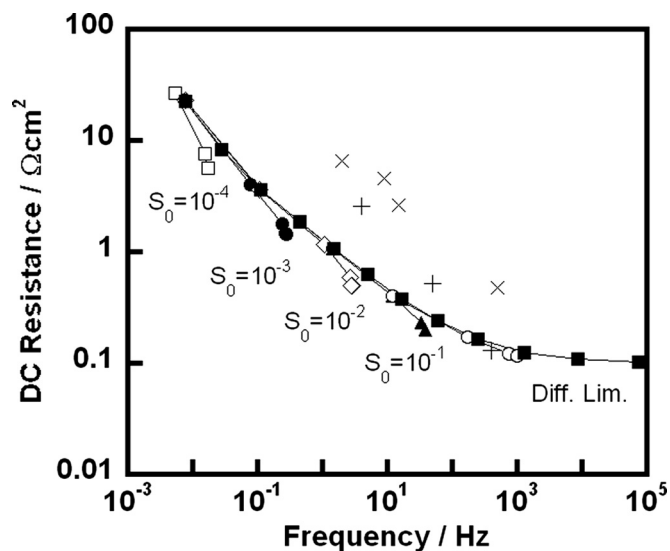
Figure 10. Calculated resistances as a function of diffusion coefficient and sticking coefficient for the non-steady state, co-limited model based on the parameters listed in Table III. Symbols correspond to (■) the purely diffusion limited case, (○) $S_0 = 10^0$, (▲) $S_0 = 10^{-1}$, (◇) $S_0 = 10^{-2}$, (●) $S_0 = 10^{-3}$, and (□) $S_0 = 10^{-4}$.

$$f = \frac{1}{2\pi R C_p} \qquad [37]$$

This characteristic frequency has been used to identify the process contributing to the impedance, with the assumption that larger frequencies correspond to electrochemical reactions and lower frequencies to diffusion processes. Figure 12 combines the data of Figs. 10 and 11, showing impedance as a function of frequency. The uppermost curve, off of which the different branches emanate, corresponds to the purely diffusion limited case. Each of the branches from the main curve represents a particular value of S_0; these branches deviate from the main curve at the point where adsorption becomes limiting for that particular S_0.

Figure 12. Calculated resistances as a function of calculated characteristic frequencies for the non-steady state, co-limited model based on the parameters listed in Table III at 973 K. Symbols correspond to (■) the purely diffusion limited case, (○) $S_0 = 10^0$, (▲) $S_0 = 10^{-1}$, (◇) $S_0 = 10^{-2}$, (●) $S_0 = 10^{-3}$, and (□) $S_0 = 10^{-4}$. Experimental data for (+) $La_{0.8}Sr_{0.2}FeO_{3-\delta}$ (Ref. 45) and (×)$La_{0.8}Sr_{0.2}MnO_{3-\delta}$ (Ref. 44) at 973 K are presented for comparison.

The characteristic frequencies in Fig. 12 agree very well with the range of frequencies observed experimentally for infiltrated LSF-YSZ (Ref. 45) and LSM-YSZ (Ref. 44) electrodes. For calcination at 1123 K, the infiltrated LSF-YSZ electrodes exhibited an impedance of 0.2 Ω cm² and a characteristic frequency of 400 Hz, which changed to 3 Ω cm² and 4 Hz after calcination to 1373 K. A selection of experimentally measured frequencies and impedances are presented for comparison as individual data points in Fig. 12.

However, one very interesting result from Fig. 12 is that the characteristic electrode frequencies are very similar for the diffusion-limited and the adsorption-limited cases. In general, the
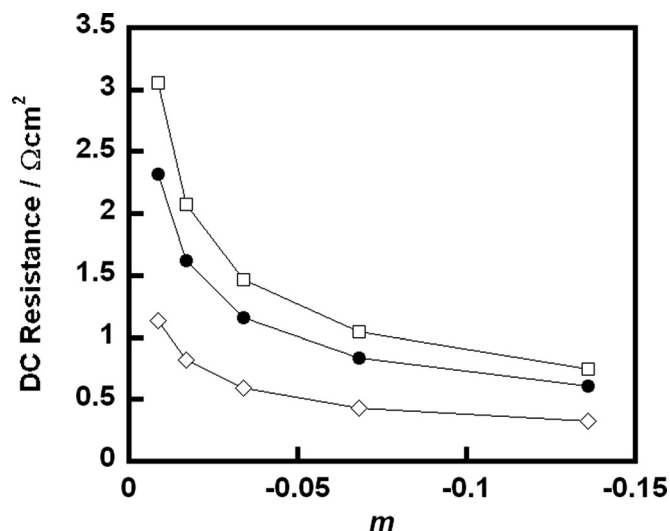

Figure 11. Calculated capacitances as a function of diffusion coefficient and sticking coefficient for the non-steady state, co-limited model based on the parameters listed in Table III at 973 K. Symbols correspond to (■) the purely diffusion limited case, (○) $S_0 = 10^0$, (▲) $S_0 = 10^{-1}$, (◇) $S_0 = 10^{-2}$, (●) $S_0 = 10^{-3}$, and (□) $S_0 = 10^{-4}$.

Figure 13. Calculated resistances as a function of the perovskite reducibility parameter, m. Impedances were calculated using the non-steady state, co-limited model based on the parameters listed in Table III at 973 K. Symbols provide examples of the(□) adsorption limited ($S_0 = 10^{-3}$, $D = 10^{-12}$ cm²/s), (●) diffusion limited ($S_0 = 10^{-2}$, $D = 10^{-13}$ cm²/s), and (◇) co-limited cases ($S_0 = 10^{-2}$, $D = 10^{-12}$ cm²/s).

frequencies for a given impedance differed by a factor of only two for the two different limiting cases. Closer inspection shows that this result should have been expected. For both diffusion and adsorption limits, the electrode capacitance results from diffusion of ions out of the perovskite film. In both cases, a step change in the overpotential requires diffusion of ions from that part of the perovskite that is in contact with the YSZ. The only difference between the two cases is that perovskite surface in contact with the gas phase remains unaffected in the diffusion-limited case but decreases over time in the adsorption-limited case. Therefore, an important consequence of the model is that the characteristic frequency does not allow one to argue which of these two processes is rate limiting.

Effect of thermodynamics on electrode performance.—It was shown in Eq. 29 that the electrode impedance for the adsorption limited case depends on the slope, m, of the equilibrium, redox isotherm for the perovskite. Using the non-steady-state model, the effect of varying m was examined for an adsorption limited, a diffusion limited, and a co-limited case. As shown in Fig. 13, increasing values of m lead to decreasing electrode resistances regardless of the limiting mechanism. This agrees with expectations from the steady-state solutions, since the substitution of Eq. 32 into Eq. 24 for the diffusion-limited case illustrates a dependence on m similar to that seen in Eq. 29 for the adsorption-limited case. This result suggests that highly reducible materials (i.e. LSCo) should provide superior performance for both the adsorption- and diffusion-limited cases. It is worth noting, however, that large values of m and high ionic conductivities are often related.

Conclusions

In this paper, we have modeled the electrode properties of electrodes formed by infiltration of perovskites into a porous layer of the electrolyte, followed by calcination to temperatures high enough for the perovskite to form a dense film of the electrolyte scaffold. Although the model is very simple, it captures the essential features that O_2 must adsorb onto the perovskite and then diffuse through the perovskite. By comparison with experimental data, the model shows that adsorption of O_2 onto the perovskite surface is likely rate limiting for perovskites with ionic conductivities greater than 10^{-7} S/cm. According to the model, electrode impedances depend strongly on the ionic conductivity of the electrolyte scaffold, the structure of the scaffold, and the slope of the perovskite oxidation isotherm. Finally, the characteristic frequency of the electrode cannot be used to determine whether diffusion or adsorption are rate limiting.

Acknowledgment

List of Symbols

A	diffusive flux prefactor
b	reducibility parameter
B	adsorption rate prefactor
C	oxygen ion concentration within the perovskite film
C_{A0}	oxygen ion concentration at equilibrium with gas phase O_2
C_0	equilibrium oxygen ion concentration at atmospheric pressure
C_P	electrode capacitance
D	oxygen ion diffusion coefficient
E	simplifying collection of constants
F	Faraday constant
f	characteristic frequency of the electrode
h	electrode thickness
h_{AR}	height of the active region
$i(y)$	current density within the YSZ fin
i_S''	charge flux entering the YSZ fin
i_0	exchange current density
J_{O2}	O_2 flux
k^*	surface exchange coefficient

L	length of repeating modeled unit
m	reducibility parameter
M	molecular weight of O_2
p	porosity
PO_{2atm}	atmospheric O_2 partial pressure
PO_{2fin}	O_2 fugacity within the YSZ fin
PO_{2surf}	O_2 fugacity at the perovskite surface
R	zero-frequencyimpedance
R_g	ideal gas constant
r_{ads}	O_2 adsorption rate
ρ	density of perovskite
ρ_{YSZ}	density of YSZ
S	sticking coefficient
S_g	specific surface area
S_0	sticking coefficient constant
T	temperature
V	volume of perovskite lattice
w	fin width
Z	characteristic length scale in z-dimension

Greek

δ	nonstoichiometry parameter
θ	percent weight loading of perovskite
λ	thickness of perovskite film
ρ	density of perovskite
ρ_{YSZ}	density of YSZ
σ_{amb}	ambipolar conductivity of the perovskite
σ_i	ionic conductivity of the perovskite
σ_{el}	electronic conductivity of the perovskite
σ_{YSZ}	bulk ionic conductivity of YSZ
σ'_{YSZ}	effective ionic conductivity of YSZ
τ	tortuosity
Φ	electrical potential
Φ_0	applied overpotential

References

1. J.M. Vohs and R. J. Gorte, *Adv. Mater.*, **21**, 943 (2009).
2. F. Tietz, Q. Fu, V. A. C. Haanappel, A. Mai, N. H. Menzler, and S. Uhlenbruck, *Int. J. Appl Ceram. Technol.*, **4**, 436 (2007).
3. S. B. Adler, *Chem. Rev.*, **104**, 4791 (2004).
4. J. Fleig and J. Maier, *J. Eur. Ceram. Soc.*, **24**, 1343 (2004).
5. S. J. Skinner, *Int. J. Inorg. Mater.*, **3**, 113 (2001).
6. M. Godickemeier, K. Sasaki, L. J. Gauckler, and I. Riess, *Solid State Ionics*, **86–88**, 691 (1996).
7. B. C. H. Steele, *Solid State Ionics*, **94**, 239 (1997).
8. F. Zhao and A. V. Virkar, *J. Power Sources*, **141**, 79 (2005).
9. R. N. Basu, G. Blass, H. P. Buchkremer, D. Stover, F. Tietz, E. Wessel, and I. C. Vinke, *J. Eur. Ceram. Soc.*, **25**, 463 (2005).
10. V. A. C. Haanappel, J. Mertens, and A. Mai, *J.Fuel Cell Sci. Technol.*, **3**, 263 (2006).
11. E. P. Murray, M. J. Sever, and S. A. Barnett, *Solid State Ionics*, **148**, 27 (2002).
12. N. T. Hart, N. P. Brandon, M. J. Day, and N. Lapena-Rey, *J. Power Sources*, **106**, 42 (2002).
13. S. B. Adler, J. A. Lane, and B. C. H. Steele, *J. Electrochem. Soc.*, **143**, 3554 (1996).
14. F. Bidrawn, S. Lee, J. M. Vohs, and R. J. Gorte, *J. Electrochem. Soc.*, **155**, B660 (2008).
15. S. Lee, M. Bevilacqua, P. Fornasiero, J. M. Vohs, and R. J. Gorte, *J. Power Sources*, **193**, 747 (2009).
16. H. Uchida, M. Yoshida, and M. Watanabe, *J. Electrochem. Soc.*, **146**, 807 (1999).
17. J. W. Erning, T. Hauber, U. Stimming, and K. Wippermann, *J. Power Sources*, **61**, 205 (1996).
18. F. Bidrawn, G. Kim, N. Aramrueang, J. M. Vohs, and R. J. Gorte, *J. Power Sources*, **195**, 720 (2010).
19. V. A. C. Haanappel, D. Rutenbeck, A. Mai, S. Uhlenbruck, D. Sebold, H. Wesemeyer, B. Rowekamp, C. Tropartz, and F. Tietz, *J. Power Sources*, **130**, 119 (2004).
20. K. J. Yoon, S. Gopalan, and U. B. Pal, *J. Electrochem. Soc.*, **156**, B311 (2009).
21. Y. X. Lu, C. Kreller, and S. B. Adler, *J. Electrochem. Soc.*, **156**, B513 (2009).
22. C. W. Tanner, K. Z. Fung, and A. V. Virkar, *J. Electrochem. Soc.*, **144**, 21 (1997).
23. B. Kenney and K. Karan, *J. Electrochem. Soc.*, **157**, B1126 (2010).
24. P. Hofmann and K. D. Panopoulos, *J. Power Sources*, **195**, 5320 (2010).
25. J. D. Nicholas and S. A. Barnett, *J. Electrochem. Soc.*, **157**, B536 (2010).
26. J. D. Nicholas and S. A. Barnett, *J. Electrochem. Soc.*, **156**, B458 (2009).
27. M. Shah, J. D. Nicholas, and S. A. Barnett, *Electrochem. Commun.*, **11**, 2 (2009).
28. D. Cui, Q. Liu, and F. L. Chen, *J. Power Sources*, **195**, 4160 (2010).
29. H. Fukunaga, M. Koyama, N. Takahashi, C. Wen, and K. Yamada, *Solid State Ionics*, **132**, 279 (2000).

30. Z. T. Xia, S. H. Chan, and K. A. Khor, *Electrochem. Solid-State Lett.*, **7**, A63 (2004).
31. J. Deseure, Y. Bultel, L. Dessemond, and E. Siebert, *Electrochim. Acta*, **50**, 2037 (2005).
32. J. Deseure, Y. Bultel, L. Dessemond, E. Siebert, and P. Ozil, *J. Appl. Electrochem.*, **37**, 129 (2007).
33. W. G. Bessler, J. Warnatz, and D. G. Goodwin, *Solid State Ionics*, **177**, 3371 (2007).
34. S. B. Adler, X. Y. Chen, and J. R. Wilson, *J. Catal.* **245**, 91 (2007).
35. F. Ciucci and D. G. Goodwin, *ECS Trans.*, **7**(1), 2075 (2007).
36. J. Fleig, *Phys . Chem. Chem. Phys.* **7**, 2027 (2005).
37. J. Fleig and J. Jamnik, *J. Electrochem. Soc.*, **152**, E138 (2005).
38. D.S. Mebane and M. Liu, *J. Solid State Electrochem.*, **10**, 575 (2006).
39. W. G. Bessler, S. Gewies, and M. Vogler, *Electrochim. Acta*, **53**, 1782 (2007).
40. J. Fleig and J. Maier, *J. Eur. Ceram. Soc.*, **24**, 1343 (2004).
41. T. Kenjo, S. Osawa, and K. Fujikawa, *J. Electrochem. Soc.*, **138**, 349 (1991).
42. S. P. Jiang, *Mater. Sci. Eng., A*, **418**, 199 (2006).
43. Y. Y. Huang, J. M. Vohs, and R. J. Gorte, *J. Electrochem. Soc.*, **151**, A646 (2004).
44. Y. Y. Huang, J. M. Vohs, and R. J. Gorte, *J. Electrochem. Soc.*, **152**, A1347 (2005).
45. W. S. Wang, M. D. Gross, J. M. Vohs, and R. J. Gorte, *J. Electrochem. Soc.*, **154**, B439 (2007).
46. H. P. He, Y. Y. Huang, J. Regal, M. Boaro, J. M. Vohs, and R. J. Gorte, *J. Am. Ceram. Soc.*, **87**, 331 (2004).
47. K.Z. Fung and A. V. Virkar, in *4th International Symposium on Solid Oxide Fuel Cells*, p. 1105, The Electrochemical Society Proceedings Series, Pennington, NJ (1995).
48. *High Temperature Solid Oxide Fuel Cells: Fundamentals, Design and Applications*, S.C. Singhal and K. Kendall, Editors, p. 240, Elsevier, New York (2003).
49. M. Paunovic and M. Schlesinger, *Fundamentals of Electrochemical Deposition*, John Wiley & Sons, New York (2006).
50. C. H. Yang, C. Jin, A. Coffin, and F. L. Chen, *Int. J. Hydrogen Energy*, **35**, 5187 (2010).
51. S.D. Ebbesen and M. Mogensen, *J. Power Sources*, **193**, 349 (2009).
52. A. Brisse, J. Schefold, and M. Zahid, *Int. J. Hydrogen Energy*, **33**, 5375 (2008).
53. P. Kim-Lohsoontorn and J. Bae, *J. Power Sources*, In Press.
54. J. E. O'Brien, C. M. Stoots, J. S. Herring, P. A. Lessing, J. J. Hartvigsen, and S. Elangovan, *J. Fuel Cell Sci. Technol.*, **2**, 156 (2005).

55. M. Liang, B. Yu, M. Wen, J. Chen, J. Xu, and Y. Zhai, *J. Power Sources*, **190**, 341 (2009).
56. F. Bidrawn, G. Kim, G. Corre, J. T. S. Irvine, J. M. Vohs, and R. J. Gorte, *Electrochem. Solid-State Lett.*, **11**, B167 (2008).
57. K. Eguchi, T. Hatagishi, and H. Arai, *Solid State Ionics*, **86–88**, 1245 (1996).
58. Y. J. Leng, S. H. Chan, K. A. Khor, and S. P. Jiang, *Int. J. Hydrogen Energy*, **29**, 1025 (2004).
59. T. Kawada, J. Suzuki, M. Sase, A. Kaimai, K. Yashiro, Y. Nigara, J. Mizusaki, K. Kawamura, and H. Yugami, *J.Electrochem. Soc.*, **149**, E252 (2002).
60. J. Mizusaki, Y. Mima, S. Yamauchi, K. Fueki, and H. Tagawa, *J. Solid State Chem.*, **80**, 102 (1989).
61. J. Mizusaki, N. Mori, H. Takai, Y. Yonemura, H. Minamiue, H. Tagawa, M. Dokiya, H. Inaba, K. Naraya, T. Sasamoto, et al., *Solid State Ionics*, **129**, 163 (2000).
62. J. Mizusaki, M. Yoshihiro, S. Yamauchi, and K. Fueki, *J. Solid State Chem.*, **58**, 257 (1985).
63. M. Sogaard, P. V. Hendriksen, and M. Mogensen, *J. Solid State Chem.*, **180**, 1489 (2007).
64. M. Sogaard, P. V. Hendriksen, M. Mogensen, F. W. Poulsen, and E. Skou, *Solid State Ionics*, **177**, 3285 (2006).
65. J. Yoo, C. Y. Park, and A. J. Jacobson, *Solid State Ionics*, **175**, 55 (2004).
66. G. Kim, G. Corre, J. T. S. Irvine, J. M. Vohs, and R. J. Gorte, *Electrochem. Solid-State Lett.*, **11**, B16 (2008).
67. S. B. Adler, *Solid State Ionics*, **111**, 125 (1998).
68. J.A. Rodriguez and D. W. Goodman, *Surf. Sci. Rep.*, **14**, 27 (1991).
69. L. Wang, R. Merkle, and J. Maier, *J. Electrochem. Soc.*, **157**, B1802.
70. W. G. Bessler, *J. Electrochem. Soc.*, **154**, B1186 (2007).
71. J.S. Yoo and S. M. Park, *Anal. Chem.*, **72**, 2035 (2000).
72. R. Jurczakowski and A. Lasia, *Anal. Chem.*, **76**, 5033 (2004).
73. J.W. Lee and S. I. Pyun, *Electrochim. Acta*, **50**, 1947 (2005).
74. Y. Ji, J. A. Kilner, and M. F. Carolan, *Solid State Ionics*, **176**, 937 (2005).
75. S. McIntosh, S. B. Adler, J. M. Vohs, and R. J. Gorte, *Electrochem. Solid-State Lett.*, **7**, A111 (2004).
76. R.A. De Souza, J. A. Kilner, and J. F. Walker, *Mater. Lett.*, **43**, 43 (2000).
77. X. D. Zhou, L. R. Pederson, J. W. Templeton, and J. W. Stevenson, *J.Electrochem. Soc.*, **157**, B220 (2010).
78. W.C. Koehler and E. O. Wollan, *J. Phys. Chem. Solids*, **2**, 100 (1957).